Local group dwarf galaxy detection limit in the CSST survey

Han Qu, Zhen Yuan, Amandine Doliva-Dolinsky, Nicolas F. Martin, Xi Kang, Chengliang Wei, Guoliang Li, Yu Luo, Jiang Chang, Chaowei Tsai, et al.

Monthly Notices of the ROYAL ASTRONOMICAL SOCIETY

MNRAS **523,** 876–886 (2023)
Advance Access publication 2023 May 8

https://doi.org/10.1093/mnras/stad1352

Local Group dwarf galaxy detection limit in the *CSST* survey

Han Qu (曲涵),[1,2]★ Zhen Yuan (袁珍),[3]★ Amandine Doliva-Dolinsky,[3] Nicolas F. Martin,[3,4] Xi Kang (康熙),[1,5] Chengliang Wei (韦成亮),[1] Guoliang Li (李国亮),[1,2] Yu Luo (罗煜),[1] Jiang Chang (常江),[1] Chaowei Tsai (蔡肇伟),[6,7,8] Zhou Fan (范舟)[6] and Rodrigo Ibata[3]

[1]*Purple Mountain Observatory, Chinese Academy of Sciences, Nanjing 210008, China*
[2]*School of Astronomy and Space Sciences, University of Science and Technology of China, Hefei 230026, China*
[3]*Université de Strasbourg, CNRS, Observatoire Astronomique de Strasbourg, UMR 7550, F-67000 Strasbourg, France*
[4]*Max-Planck-Institut für Astronomie, Königstuhl 17, D-69117, Heidelberg, Germany*
[5]*Zhejiang University-Purple Mountain Observatory Joint Research Center for Astronomy, Zhejiang University, Hangzhou 310027, China*
[6]*National Astronomical Observatories, Chinese Academy of Sciences, 20A Datun Road, Chaoyang District, Beijing 100012, China*
[7]*Institute for Frontiers in Astronomy and Astrophysics, Beijing Normal University, Beijing 102206, China*
[8]*School of Astronomy and Space Science, University of Chinese Academy of Sciences, Beijing 100049, China*

Accepted 2023 April 27. Received 2023 March 30; in original form 2022 December 20

ABSTRACT

We predict the dwarf galaxy detection limits for the upcoming *Chinese Space Station Telescope (CSST)* survey that will cover 17 500 $\deg^2$ of the sky with a wide field of view of 1.1 $\deg^2$. The point-source depth reaches 26.3 mag in the *g* band and 25.9 mag in the *i* band. Constructing mock survey data based on the designed photometric bands, we estimate the recovery rate of artificial dwarf galaxies from mock point-source photometric catalogues. The detection of these artificial dwarf galaxies is strongly dependent on their distance, magnitude, and size, in agreement with searches in current surveys. We expect *CSST* to enable the detection of dwarf galaxies with $M_V = -3.0$ and $\mu_{250} = 32.0$ mag arcsec^{-2} (surface brightness limit for a system of half-light radius $r_h = 250$ pc) at 400 kpc, and $M_V = -4.9$ and $\mu_{250} = 30.5$ mag arcsec^{-2} around the Andromeda galaxy. Beyond the Local Group, the *CSST* survey will achieve $M_V = -5.8$, and $\mu_{250} = 29.7$ mag arcsec^{-2} in the distance range of 1–2 Mpc, opening up an exciting discovery space for faint field dwarf galaxies. With its optical bands, wide survey footprint, and space resolution, *CSST* will undoubtedly expand our knowledge of low-mass dwarf galaxies to an unprecedented volume.

Key words: Galaxy: halo – galaxies: dwarf – Local Group.

1 INTRODUCTION

Within the paradigm of hierarchical structure formation, massive galaxies grew through the absorption of low-mass systems, most of which are dwarf galaxies (Lacey & Cole 1993; Vogelsberger et al. 2014). In the Local Group, some of these building blocks survive until now and become satellites of the Milky Way (MW) and the Andromeda galaxy (M31). The number of these dwarf galaxies can provide tests for cosmological models, as well as constraints on baryonic physics that governs galaxy evolution (Bovill & Ricotti 2009, 2011; Phillips et al. 2015; Bullock & Boylan-Kolchin 2017).

Significant progress has been made in searching dwarf satellite galaxies around the MW-M31 pair in recent years (Walsh, Jerjen & Willman 2007; Walsh, Willman & Jerjen 2009; Martin et al. 2013; Bechtol et al. 2015; Drlica-Wagner et al. 2015; Koposov et al. 2015; Laevens et al. 2015a,b; Simon 2019). Up to now, nearly 100 dwarf galaxies have been detected in the Local Group: 59 in the MW with $M_V < -0.8 \pm 0.9$ and 39 in M31 with $M_V < -5.9 \pm 0.7$ thanks to the large scale digital survey including the Sloan Digital Sky Survey (SDSS; Abazajian et al. 2003), the Dark Energy Survey (DES; Abbott et al. 2018), the Pan-STARRS survey (Chambers et al. 2016), or the Pan-Andromeda Archaeological Survey (McConnachie et al. 2018).

In the era of optical and near-infrared wide surveys constructed with space telescopes (e.g. Roman, Spergel et al. 2015; Wallner et al. 2017), the *Chinese Space Station Telescope (CSST)* survey is planned to perform both photometric imaging and slitless spectroscopic observations and will cover 17 500 $\deg^2$ in its planned 10 yr of operation (Zhan 2011; Cao et al. 2018; Gong et al. 2019). The *CSST* is a 2-m space telescope and shares the same orbit as the Chinese Space Station, which will be launched in the next few years. The main survey camera module has a large field of view (1.1 $\deg^2$), a high spatial resolution (∼0.15 arcmin), and is equipped with a set of near-ultraviolet to near-infrared filters (*NUV* and *ugrizy*). The instrumental design of the *CSST* makes it an optimal tool to search for low-mass/faint dwarf galaxies within the Local Volume. In this paper, we make the first predictions of the detectability of dwarf galaxies within 2 Mpc from mock photometric catalogues.

The paper is structured as follows: In Section 2, we estimate the completeness and photometric uncertainties of point-source detections with *CSST*. Based on that, we construct a series of mock catalogues by injecting artificial dwarf galaxies in the modelled contamination from MW foreground stars. The dwarf galaxy search algorithm is explained in Section 3. The results from applying this algorithm to the mock catalogues are discussed in Section 4, in which we compare the detection limits of the *CSST* survey with limits from existing surveys and the known Local Group dwarf galaxies. Section 5 closes the paper with a summary and discussion.

★ E-mail: qvhan@pmo.ac.cn (HQ); zhen.yuan@astro.unistra.fr (ZY)

Table 1. Designed Parameters of *CSST*.

Survey characteristics							
Wide survey	15 000 deg^2 (|b|>20°) + 2500 deg^2 (15°<|b|<20°)						
Deep survey	400 deg^2 (selected areas)						
Photometric System							
Band	*NUV*	*u*	*g*	*r*	*i*	*z*	*y*
Wavelength (λ_{-90}−λ_{+90} nm)	255–317	322–396	403–545	554–684	695–833	846–1065	937–1065
Wide imaging (5σ depth)	25.4	25.4	26.3	26.0	25.9	25.2	24.4
Deep imaging (5σ depth)	26.7	26.7	27.5	27.2	27.0	26.4	25.7

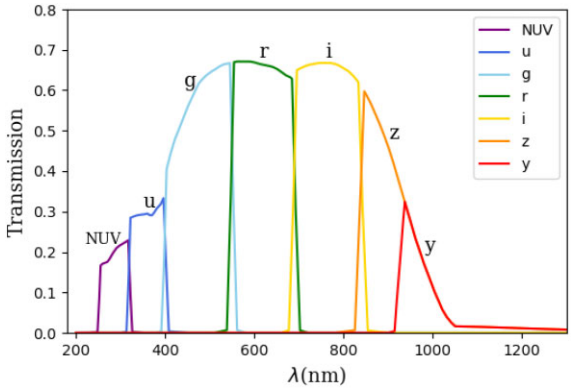

Figure 1. Transmission curves of the seven *CSST* filters, covering wavelengths from the near ultraviolet, to the near-infrared (*NUV*, *u*, *g*, *r*, *i*, *z*, and *y* bands).

2 MOCK DATA

2.1 The *CSST* imaging survey

The *CSST* wide imaging survey has a sky coverage of 17 500 deg^2 (42.4 per cent of the whole sky), and 400 deg^2 of this area will be selected for the deep survey (see details in Table 1). The designed photometric system has seven broad-band filters, *NUV*, *u*, *g*, *r*, *i*, *z*, and *y*, that cover the full 255–1065 nm range, from the near-ultraviolet (*NUV*) to the near-infrared (*y*). The transmission curves of the filters are shown in Fig. 1 and listed in Table 1. For the wide survey, the survey depth is reached with two 150-second exposures for the *u*, *g*, *r*, *i*, and *z* bands, and four such exposures for the *NUV* and *y* bands. The final products will correspond to stacked images whose photometric catalogues will, ultimately, reach the following 5σ point-source limiting magnitudes: 25.4 (*NUV*), 25.4 (*u*), 26.3 (*g*), 26.0 (*r*), 25.9 (*i*), 25.2 (*z*), and 24.4 (*y*) in the AB system (see Table 1; e.g. Cao et al. 2018).

In this work, we estimate the completeness and photometric uncertainties of point-source detections as a function of magnitude based on the designed parameters of the *CSST* (Zhan 2011; Cao et al. 2018). First, we use the *CSST* Image Simulator to produce mock optical images of stars for a single 150-second exposure. The catalogue consists of stars brighter than $G = 21$ from *Gaia* DR2 and fainter MW stars simulated using the GALAXIA model (Sharma et al. 2011), a fast code for creating a synthetic survey of the MW (see more details in Section 2.2.1). We then perform source detection and photometric measurements on the mock images using SEXTRACTOR (Bertin & Arnouts 1996). The completeness functions of point sources are shown in the left-hand panel of Fig. 2, with the results for a single-exposure shown as dashed lines for the *g* and *i* bands (blue and red, respectively). For the nominal double-exposures depth, we shift those models by 0.38 mag (solid lines). In the single-exposure mode, the detection limits (defined as the magnitudes at which the completeness drops to 70 per cent) are $g_{\rm lim} = 26.0$ and $i_{\rm lim} = 25.5$. Note that we assume star and galaxy can be separated 100 per cent for point-source detections to the survey depth. The estimates of the successful rate of star galaxy separation using different models as well as its impact on the dwarf galaxy detection will be investigated in future work.

The photometric uncertainties in each band are estimated from the same images. We first measure the magnitude of a detected object by processing mock images with SEXTRACTOR, then compare it with the true magnitude from the input catalogue that is given to the *CSST* Image Simulator. The uncertainty is described using the difference between the measured and the input values as a function of magnitude (see right-hand panel of Fig. 2). In the single-exposure mode, uncertainties reach ∼0.2 mag around $g = 25.5$ and $i = 24.7$. We model the measured uncertainties with the following model:

$$\delta(M) = a + \exp(bM - c), \quad (1)$$

with $\delta(M)$ the uncertainty, M the magnitude, and (a, b, c) the coefficients we fit for. Based on the measured uncertainties, we find $(a, b, c) = (0.015, 0.736, 20.423)$ and $(0.026, 0.827, 22.144)$ for the *g* and *i* bands, respectively. The resulting fits are shown in Fig. 2. These are for a single *CSST* image so, to account for the double-exposure mode that will be used for these two bands, we simply shift those models by 0.38 mag.

2.2 Mock catalogue

With the completeness and photometric uncertainty functions of point-source detection in hand, we now construct mock catalogues in the *CSST* bands by injecting artificial dwarf galaxies in the foreground MW model. In this work, we aim to explore the detection efficiency of dwarf galaxies with *CSST* from a series of mock catalogues by varying five key parameters: the absolute magnitude (M_V), distance (D), and the half-light radius ($r_{\rm h}$) of an artificial dwarf galaxy, the MW foreground parametrized by the Galactic latitude b, and the survey depth with single and double exposures.

2.2.1 *Milky Way foreground*

The mock MW foreground catalogue is generated by GALAXIA. It uses a Galactic model that is initially based on the Besançon model (Robin et al. 2003), as well as realistic substructure of the stellar halo based on N-body simulations (Bullock & Johnston 2005). The MW model used in this work includes a metal-rich thick disc correction with [Fe/H] from −0.78 to −0.16 according to Sharma et al. (2019).

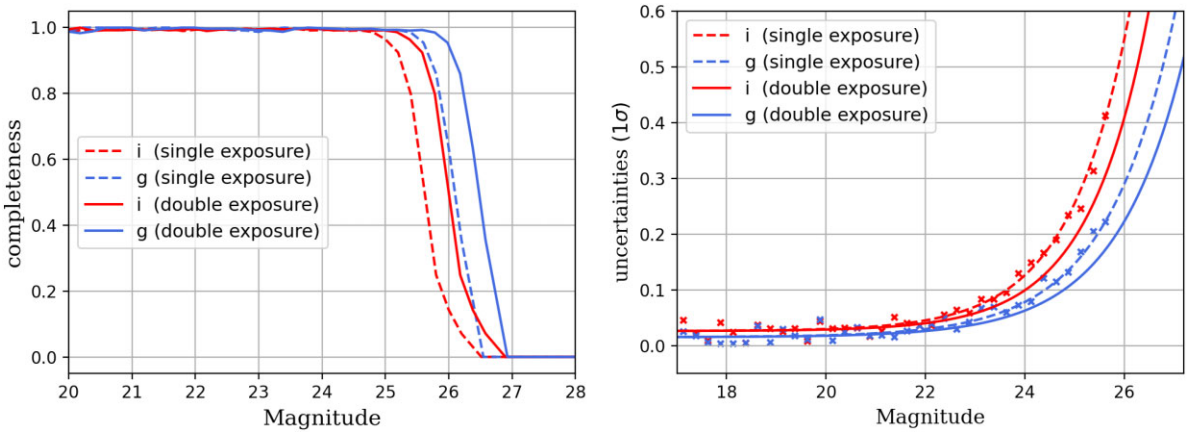

Figure 2. Left: Completeness model for point-source detections as a function of *g* (blue) and *i* (red) magnitude estimates for the *CSST*. The dashed and solid lines represent the single- and double-exposure modes, respectively. Right: Expected photometric uncertainties in the two bands for the one-exposure model (crosses) and fitted model (dashed lines). The two-exposure uncertainty model (full lines) corresponds to a shift of these models by 0.38 mag to account for the increased exposure time.

Since the MW foreground is more crowded close to the Galactic disc, we generate three different MW fields that aim to represent the varying contaminating conditions in the *CSST* survey. Labelled 'L', 'M', and 'H', they represent large sky areas centred on location at low ($b = 25°$), median ($b = 45°$), and high ($b = 70°$) Galactic latitudes (see details in Table. 2).

2.2.2 *Artificial dwarf galaxy*

Most of the known dwarf galaxies in the Local Group are old and very metal-poor because of their ancient and relatively short star formation histories. In this work, we generate a group of artificial dwarf galaxies that host a single stellar population randomly drawn from the age range 8–13 Gyr. Taking into account the mass–metallicity relationship observed from the satellite dwarf galaxies (e.g. Kirby 2009), we set a range of metallicities $-1.7 <$ [Fe/H] < -1.5 for dwarf galaxies with $M_V \lesssim -7$ (stellar mass $\gtrsim 2 \times 10^5$ M$_\odot$), and $-2.2 <$ [Fe/H] < -1.7 for dwarf galaxies with $M_V \gtrsim -7$ (stellar mass $\lesssim 2 \times 10^5$ M$_\odot$). With the age and metallicity of a dwarf galaxy chosen, the stellar parameters and luminosity function of this population are generated by the Padova and Trieste Stellar Evolution Code (PARSEC) library (Bressan et al. 2012).[1] We then use GALEVNBD to generate *CSST* photometric bands based on these stellar parameters by convolving theoretical spectra with the response function of each filter (Pang et al. 2016).

The artificial dwarf galaxies are assumed to follow a typical projected radial density profile (Doliva-Dolinsky et al. 2022), characterized by the half-light radius r_h of the system. The probability density function of stars as a function of the on-sky radius, $P(r)$, is defined as

$$P(r) = \frac{1.68^2 r}{2\pi r_h^2} \exp\left(-1.68\frac{r}{r_h}\right). \quad (2)$$

We further flatten this distribution so it has ellipticity $e = 1-(b/a)$, with a and b the major and minor axis scale lengths, respectively.

The process to generate an artificial dwarf galaxy is visualized in Fig. 3 for $M_V = -4.5$, [Fe/H] $= -2.2$, age $= 10$ Gyr, $D = 255$ kpc, at high Galactic latitude ($b = 43°$), and for the double-exposure mode. Panels (a) to (e) show how the colour–magnitude diagram (CMD) of the system in constructed and panels (f) and (g) show its on-sky projection. Stars are first drawn from the galaxy's isochrone and corresponding luminosity function of chosen age, metallicity, and distance until the absolute magnitude of the system reaches the target M_V (a). The CMD is then convolved by the photometric uncertainties (b) and the completeness model of *CSST* is applied (c). In (d), we combine the dwarf galaxy stars (blue) and the MW foreground stars (grey, see also panel e) within $2r_h$ at $(l, b) = (67.6°, 43°)$. The spatial distribution of the dwarf galaxy stars are shown in panel (f) in coordinates of the plane tangent to the sky, and as they would appear in the data in panel (g).

Following this procedure, we construct a large series of mock dwarf galaxies in the range of $-10.0 < M_V < +2.0$ with steps of 0.5 log (r_h/*pc*), and 3 pc $< r_h <$ 3 kpc with steps of 0.25 log (r_h/*pc*). Distances are set within the range $32 < D < 2048$ kpc (see details in Table 2) and the ellipticity of the dwarf galaxy is randomly sampled between $0.3 < e < 0.7$.

Mock catalogues are generated for the six different combinations of the three MW fields (L, M, H) and the two survey depths (single and double exposures). For each combination of these parameters, we generated 10 140 mock dwarf galaxies with three varying parameters (M_V, D, and r_h), and ingested them in the MW contamination catalogue in 20 different batches of ∼500 galaxies each to avoid an overlap between the galaxies. In total, we simulate 60 840 artificial galaxies.

3 SEARCH ALGORITHM

The dwarf galaxy search algorithm used in this work was described in Walsh et al. (2009) and has been widely adopted, for instance to explore the data from the SDSS (Walsh et al. 2007; Koposov et al. 2008), the DES (Bechtol et al. 2015; Drlica-Wagner et al. 2015; Koposov et al. 2015), Pan-STARRS (Laevens et al. 2015a,b), Hyper Suprime-Cam Subaru Strategic Program (Homma et al. 2018), and the Wide component of the DECam Local Volume Exploration Survey (Mau et al. 2020). Following the approach of Koposov et al. (2008), Walsh et al. (2009), Bechtol et al. (2015), and Homma et al. (2019), our version of the algorithm works as follows: For a given distance choice, we start by selecting stars that fall within a CMD selection box constructed from isochrones that represent the dominant stellar populations observed in dwarf galaxies. Specifically,

[1] http://stev.oapd.inaf.it/cgi-bin/cmd

Table 2. Chosen parameter ranges for the artificial dwarf galaxies and detection thresholds.

Artificial dwarf galaxy			
Parameter	Minimal	Maximal	Step (log scale)
MV	−10.0	2.0	0.5
r_h (pc)	3.16	3162	0.25
D (kpc)	32	2048	1

Detection threshold of each field							
Field	l (°)	b (°)		Depth	$\sigma' = 2$	$\sigma' = 4$	$\sigma' = 8$
L (low)	35−85	15−35	S/N_{thr}	single exposure, double exposure	6.2, 6.6	5.5, 5.3	5.2, 5.0
M (median)	40−100	30−60		single exposure, double exposure	6.5, 6.1	5.6, 5.0	4.7, 5.0
H (high)	10−160	60−80		single exposure, double exposure	6.3, 6.3	5.3, 5.2	5.7, 5.4

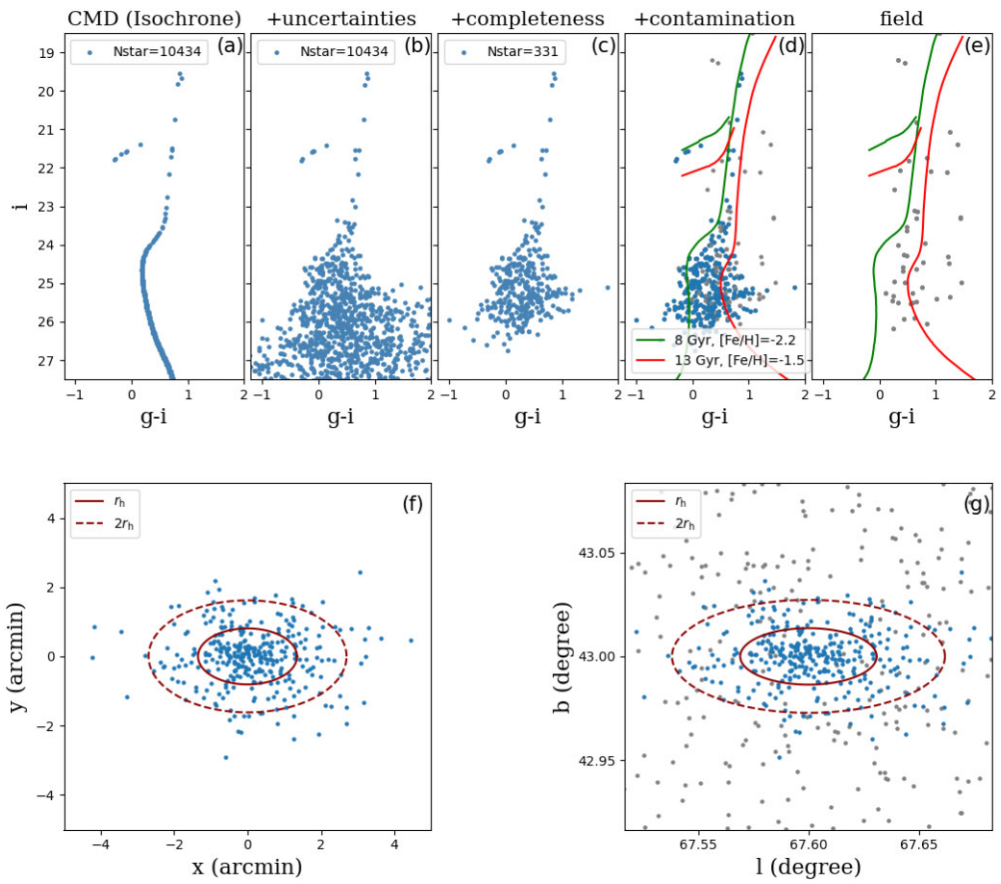

Figure 3. Process of generating an artificial dwarf galaxy in the CMD (a)–(e) and on the sky panels (panels f and g). Panel (a): a sample of 10 434 stars drawn from the isochrone of a single stellar population ($M_V = -4.5$, [Fe/H] $= -2.2$, age $= 10$ Gyr). Panel (b): same as (a) after taking into account the photometric uncertainties. Panel (c): same (b) after folding in the completeness model. Panel (d): the final CMD of the artificial dwarf galaxy within $2r_h$, combined with MW foreground stars over the same region (grey). The latter are plotted separately in panel (e) for comparison. The green and red lines represent the isochrones used to define the CMD selection box use by the search algorithm. Panel (f): the 2D spatial distribution in the Cartesian coordinates of stars from a dwarf galaxy with $r_h = 100$ pc at the distance of 255 kpc. The ellipsis correspond to 1 and $2r_h$ (solid and dashed lines, respectively). Panel (g): the stars from (f) after their ingestion in the median latitude MW field.

we choose two single populations with age = 8 Gyr, [Fe/H] = −2.2 and age = 13 Gyr, [Fe/H] = −1.5, shown as the green and red lines in Fig. 3, panels (d) and (e). The two isochrones are shifted left (blue) and right (red) by 0.05 mag along the *g*–*i* colour axis to form the contours, which are further widened by taking into account the photometric uncertainties. Stars located within the selection box are used to build binned density maps on the sky, $I(i)$, using HEALPIX (Górski et al. 2005). These density maps of stars on the sky are then convolved with a Gaussian kernel $g(i, \sigma)$ of dispersion σ to produce smoothed maps

$$L(i, \sigma) = I(i) \otimes g(i, \sigma). \quad (3)$$

An efficient way to optimize the search for dwarf galaxies is to perform this convolution with a kernel of the size σ_2 of the signal one is looking for, and subtract from it a map convolved by a much larger kernel, σ_1. The latter map will account for a smoothly varying contamination and optimize the resulting signal to noise (S/N). The resulting signal map is therefore

$$\Delta L(i)_{\sigma_1,\sigma_2} = L(i,\sigma_2) - L(i,\sigma_1). \quad (4)$$

Following Koposov et al. (2008), we use three sets of (σ_1, σ_2) kernels: (28, 2 arcmin), (28, 4 arcmin), and (56, 8 arcmin). The three different σ_2 correspond to the angular sizes of a dwarf galaxy with $r_h = 100$ pc at different distances (i.e. 40 kpc, 100 kpc, and 200 kpc). We tailor the background kernel σ_1 such that it is at least seven times larger than σ_2 to optimize the computing time. For the same reason, we bin the starting map I using 0.5 arcmin pixels when $\sigma_2 = 2$ or 4 arcmin and we use 2.0 arcmin pixels when using the larger kernels.

To evaluate the significance of local overdensities, we define the standard deviation $s(i)$ at the i-th pixel in the differential density map $\Delta L(i)$ as

$$s(i)^2 = \langle|\Delta L(j)_{\sigma_1,\sigma_2}|^2\rangle_{r_1,r_2} - |\langle\Delta L(j)_{\sigma_1,\sigma_2}\rangle_{r_1,r_2}|^2, \quad (5)$$

with $\langle\,.\,\rangle_{r_1,r_2}$ the average over pixels within a ring around the i-th pixel between $r_1 = 0.5^\circ$ and $r_2 = 1^\circ$. The standard deviation $s(i)$ of the differential density map evaluates the Poisson noise for the i-th pixel, and thus the significance of the overdensity is defined as

$$S/N(i) = \Delta L(i)/s(i). \quad (6)$$

To systematically search for the stellar overdensities resulting from dwarf galaxies with a variety of physical scales and distances, we follow the procedure described above for different distance assumptions by shifting the CMD selection box with distance moduli between 18.0 (40 kpc) and 26.5 (2 Mpc), with steps of 0.5 mag. After convolving these maps with three different kernel sets, we obtain $18 \times 3 = 54$ S/N maps.

These different maps have different noise properties. To evaluate these S/N maps on the same scale, we stack the 18 maps with the same sets of kernels but at different distances by simply taking their average, and obtain three 'master S/N map'. This step is also applied to the empty fields when determining the detection threshold in Section 4.1. We then rescale each master map to generate the final master maps, S/N_r, by subtracting the mean pixel value of each map, $\langle S/N\rangle$, and normalizing with their standard deviation, $\sigma_{S/N}$, i.e.

$$S/N_r(i) = \frac{S/N(i) - \langle S/N\rangle}{\sigma_{S/N}}. \quad (7)$$

Each pixel in these three master maps, corresponding to the three choices of kernels, now expressed the significance of a detection and we search for pixels with high S/N_r in each of the three master maps as candidate detections of dwarf galaxies.

4 APPLICATION TO THE MOCK DATA

4.1 Detection threshold

The application of the search algorithm described above to the mock catalogues results in three master maps, one for each set of kernels. We now need to decide on what constitutes a detection in those maps. It means determining the detection threshold above which we consider a detection reliable and significantly above noise fluctuations. This detection threshold, S/N_{thr}, is calculated from the estimate of the Poisson fluctuations of maps generated from the mock MW foreground alone (i.e. without the ingestion of any artificial dwarf galaxies), S/N_{MW}.

We first generate 2000 MW sky patches of 15 deg^2 for the six combinations of Galactic latitudes (L, M, H) and exposure time (single- and double-exposure modes). We apply the same search algorithm from Section 3 to these empty fields for each distance moduli. For each patch, we first obtain 18 S/N maps of MW foreground and then $S/N_{MW,r}$ after stacking them. Fig. 4 shows the distributions of the maximum values of these rescaled maps, $S/N_{MW,max}$ of 2000 patches in each combination, with the black vertical line denoting their mean value, $\langle S/N_{MW,max}\rangle$. The stacking process averages the noises at different distances that reduces the effect from outliers and eventually leads to more successful detection rate. Since we did not add any artificial dwarf galaxy in these mocks, we use them to determine the threshold value of a detection, S/N_{thr}, such that the number of false positives is below 1/500, ensure that most of the detections correspond to meaningful objects without being overly conservative. Theoretically, this corresponds to setting $S/N_{thr} = 1.25\langle S/N_{MW,max}\rangle$. For the 18 000 S/N_{MW} we simulate, this corresponds to an expected 32 false detections and a low contamination rate of less than 0.17 per cent. We are, therefore, confident that the chosen detection threshold does not bias our results and does not lead to detection limits that are too aggressive.

To verify our method, we applied the search algorithm to the public DES catalogues in a sky area of $\sim 14^\circ \times 13^\circ$ containing four newly discovered dwarf galaxies (Tucana III, Tucana V, Phoenix 2, and Tucana 2; Drlica-Wagner et al. 2015; Koposov et al. 2015), out of which Phoenix 2 ($M_V = -2.8 \pm 0.2$ at 83 kpc) is close to the detection limit of DES at its distance. Following the above steps, all four galaxies have derived S/N above the detection thresholds of a M field listed in Table 2.

4.2 Results

The resulting dwarf galaxy detection fractions for field M is shown in Fig. 5. The different panels represent separate distance bins spanning the range from 32 kpc to 2 Mpc. The pixel size in the $[M_V, \log_{10}(r_h)]$ plane is (0.5, 0.25), and each pixel contains 10 galaxies. The grey levels represent the detection fraction in each pixel, with white and black pixels denoting 0 per cent and 100 per cent detection probabilities, respectively. Following previous work (e.g. Koposov et al. 2008; Doliva-Dolinsky et al. 2022), we aim to fit an analytic model to these detection fractions to bypass the noise that is generated from testing only 10 dwarf galaxies per pixel. The transition region between full recovery and no recovery shows a 'knee' feature: at faint magnitudes, the transition region is vertical for small half-light radii, before correlating with the radii at brighter magnitudes. We understand this behaviour as follows. A minimum number of stars is required for a system to produce a detection for a given choice of detection threshold, irrespective of the size of this system. This effect produces the vertical part of the transition region with a fixed M_V limit for the lower values of $\log(r_h)$. The sloped part of the transition region is more directly related to the surface brightness of the system and the recovery fraction in this region is therefore a function of both size and luminosity. These two different parts of the transition region also have different widths between the no and full detection modes.

We adopt an analytical model to characterize the recovery fractions as a function of M_V and $\log_{10}(r_h)$, similarly to what was done by Koposov et al. (2008), Drlica-Wagner et al. (2020), or Doliva-Dolinsky et al. (2022). We parameterize the transition region with

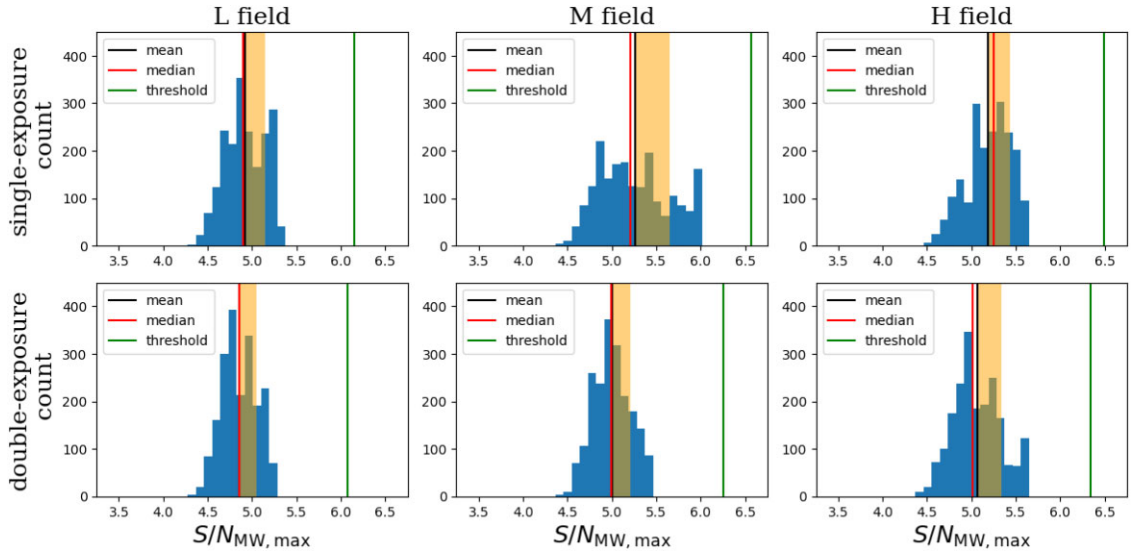

Figure 4. Distribution of $S/N_{MW,max}$ from 2000 S/N_{MW} maps with the set of ($\sigma_1 = 28$ arcmin, $\sigma_2 = 2$ arcmin) in the L, M, and H fields. The black and red lines denote the mean and median values of $S/N_{MW,max}$, respectively and the orange band represents the standard deviation of the distribution. The green line marks the position of S/N_{thr}.

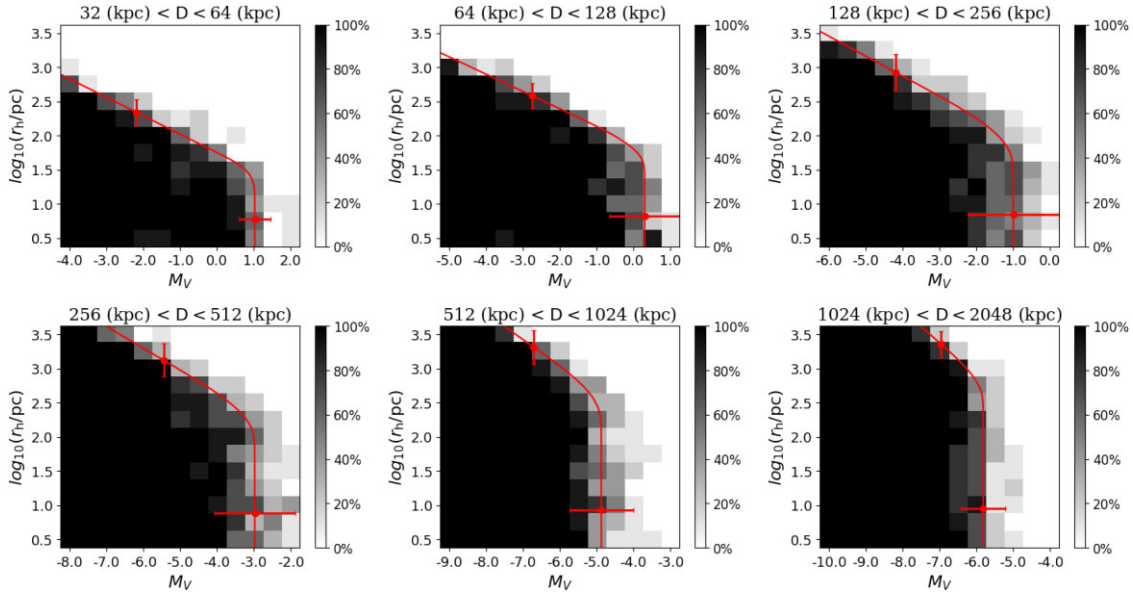

Figure 5. Detection fraction map as a function of luminosity and size in different distance bins for M field, where the black pixels indicate 100 per cent detection fraction, and the white ones indicate 0 per cent. The red curve corresponds to the modelled 50 per cent recovery fraction and the error bars represent σ_M and σ_r as the widths of the transition regions.

the following equation,

$$M_V = \begin{cases} M_{V,\mathrm{lim}} & r_\mathrm{h} < r_0 \\ \beta(\log_{10}(r_0) - \log_{10}(r_\mathrm{h})) + M_{V,\mathrm{lim}} & r_\mathrm{h} > r_0, \end{cases} \quad (8)$$

with $M_{V,\mathrm{lim}}$ the value of M_V for the vertical part of the model, r_0 the half-light radius of the knee, and β the slope of the sloped part of the model.

To model the width of the transition region, we further introduce $F(x) = \mathrm{erfc}(x/\sqrt{2})/2$ and define the model recovery fraction as

$$f(M_V, \log_{10}(r_\mathrm{h})) = F\left(\frac{\Delta M_V}{\sigma_M}\right) F\left(\frac{\Delta \log_{10}(r_\mathrm{h}))}{\sigma_r}\right). \quad (9)$$

Here, ΔM_V is the distance along the M_V axis from the transition model of equation (8) for $\log_{10}(r_\mathrm{h}) < \log_{10}(r_0)$ and $\Delta\log_{10}(r_\mathrm{h})$ is the distance along the $\log(r_\mathrm{h})$ axis for $\log_{10}(r_\mathrm{h}) > \log_{10}(r_0)$. σ_M and σ_r represent the width of the transition regions for these two parts of the recovery fraction space, respectively.

With these definitions, the model has five parameters, ($M_{V,\mathrm{lim}}$, $\log_{10}(r_0)$, β, σ_M, and σ_r), which we fit for in all the recovery fraction spaces that we have calculated by minimizing residuals between the model and the data in the 5-dimensional space. The red solid lines in each panel of Fig. 5 show the line of 50 per cent recovery fraction for the best fits and the error bars (σ_M and σ_r) represent the interval between 16 per cent and 84 per cent detection fractions. The parameters for best-fitting model are listed in Table A1–A3 in the Appendix.

Fig. 6 summarizes the recovery fraction models in the size-luminosity and surface brightness–luminosity planes, for field M in different distance bins, and for the single- (dashed lines) and double-exposure models (full lines). The horizontal and vertical error bars denote the width of the transition region between full and no detection, i.e. $\sigma_{\rm M}$ and $\sigma_{\rm r}$ from equation (9). We note that, as pointed out by Doliva-Dolinsky et al. (2022), that the detection limits do not follow lines of constant surface brightness, even for brighter luminosity than the knee (right-hand panel), and should warn us against using simple surface-brightness cuts to summarize dwarf galaxy detection limits. It is likely the consequence of the complex search algorithm and is a common feature of such procedures (e.g. Drlica-Wagner et al. 2020).

We obtain similar results for the other two MW fields, L and H see Figs A1, A2, and Fig. 7 presents a summary of the detection limits as a function of distance for the three MW fields and the two exposure configurations. In the top row of panels, $M_{V,\rm lim}$ corresponds to the vertical part of the models presented in Figs 5 and 6. In the bottom row of panels, $\mu_{250,\rm lim}$ is the value of the detection limit model at a fixed radius[2] $\log_{10}(r_{\rm h}) = 250$ pc. In all panels, the lighter/darker coloured curve represents the detection limit for the single/double-exposure mode. The shaded bands denote the width of the transition region that was represented by error bars in Fig. 6. As expected, changing integration times from 150 to 300 s yields a small but clear improvement to the detection limits, shifting them to ∼0.5 mag fainter. There is also a small impact of the MW contamination, with $M_{V,\rm lim}$ moving to slightly fainter magnitudes as the Galactic latitude increases. Similarly, $\mu_{250,\rm lim}$ only marginally changes with latitude. The artificial dwarf galaxies generated in this study are old and metal-poor. Although we expect to find more dwarf galaxies with recent star formation in the field of the Local Group, they are easier to be identified from their young blue stellar populations. Therefore, we quantify the detectability of the *CSST* using only the old dwarf galaxies.

Fig. 8 compares the predicted *CSST* detection limits with the properties of known Local Group satellites, including the lowest surface brightness systems that were only recently discovered in the deepest current survey, the Hyper Suprime-Cam Subaru Strategic Program (HSC-SSP). These three satellites, Virgo I, Cetus III, and Boötes IV (Miyazaki et al. 2012; Homma et al. 2016, 2018) located at $D = 91$ kpc, 251 kpc, and 209 kpc and with $M_V = -0.3$, -2.4, and -4.5 are the typical kind of the systems that the *CSST* survey should be able to uncover easily. These satellites are about 2 mag fainter than the faintest dwarf galaxies discovered in the previous generation of surveys (SDSS, DES, and Pan-STARRS). Even in the case of M31, whose satellite dwarf galaxies were mainly discovered in the data from the PAndAS survey that is deeper than these other surveys, *CSST* should be able to uncover new systems that are fainter than the currently known ones, further populating the faint end of M31's dwarf galaxy system.

For a more quantitative comparison, the detection limits of $M_{V,\rm lim}$ and $\mu_{250,\rm lim}$ are summarized in Table 3, with the assumption of double exposures in the M field, at different distances. In particular, if we compare those with the DES and Pan-STARRS detection limits Drlica-Wagner et al. (2020), we find that, at the distance of 400 kpc, the detection limits of these surveys that led to the discovery of numerous satellites are $M_{V,\rm lim} = -4.5$ (DES; equivalent to $\sim 6 \times 10^3\,{\rm M}_\odot$) and -6.5 (PS1), while the *CSST* survey should yield $M_{V,\rm lim} = -3.0$ (equivalent to $\sim 1.6 \times 10^3\,{\rm M}_\odot$). At this distance, the surface brightness limits reach $\mu_{250,\rm lim} = 29.9$ mag arcsec^{-2} (DES) and 28.1 mag arcsec^{-2} (PS1), compared to $\mu_{250,\rm lim} = 32.0$ mag arcsec^{-2} for *CSST*. In the case of the M31 satellites, we use our results for field L and 512–1024 kpc results (M31 is located at $b = -21.6^\circ$ and $D \sim 780$ kpc) for comparison with the detailed study of Doliva-Dolinsky et al. (2022) for PAndAS. They find $\mu_{250,\rm lim} \geq 30.0$ mag arcsec^{-2} in regions without much contamination from M31's stellar halo substructure, while our analysis yields a slight improvement with $\mu_{250,\rm lim} \geq 30.5$ mag arcsec^{-2}.

Compared to other space-based telescope programs, e.g. *Euclid* has similar survey depths, 26.2 for the visible band and 24.5 for near-infrared bands (Euclid Collaboration 2022). Roman is designed to reach almost 27 for infrared bands (Akeson et al. 2019). The filter system design *CSST* has the narrowest bandwidth as well as the bluest wavelength coverage. Compared the ground-based telescope program, the Legacy Survey of Space and Time (LSST) has the expected full depth of g ∼ 27.4 after 10 yr of survey (Ivezić et al. 2019). The *CSST* is less deep (g ∼ 26.3) but has a better angular resolution, which is critical to separate stars and galaxies from faint sources. From all of the above, the designed *CSST* features are competitive to search for old and metal-poor star populations from dwarf galaxies. It will open the realm of efficient searches for dwarf galaxies beyond the Local Group and should, for instance, enable the discovery of very faint dwarf galaxies in the field. In the most distant bin (1–2 Mpc) explored in this work, we predict that the detection limits are $M_{V,\rm lim} = -5.8$ and $\mu_{250,\rm lim} = 29.7$ mag arcsec^{-2} for the *CSST*.

5 SUMMARY

In this work, we determine the detection limits of finding dwarf galaxies within 2 Mpc with the upcoming wide photometric survey that will be observed by the *CSST*. We estimate the completeness of point-source detections and uncertainties in each photometric band and use these to construct mock catalogues in the *CSST* bands of artificial dwarf galaxies ingested in modelled MW foreground. From the application of a well-established search algorithm, we calculate the recovery fraction of dwarf galaxies in the (M_V, $r_{\rm h}$) space at different distances ranging from 32 kpc to 2 Mpc. We show that the *CSST* is able to push the frontier of dwarf galaxy searches and detect fainter objects than currently known around the MW-M31 pair or, beyond, in the field. The surface brightness of most of the known MW satellites is brighter than 32.0 mag arcsec^{-2}, whereas the *CSST* survey will open the realm of fainter systems, down to $\mu_{250,\rm lim} \sim 33.0$ mag arcsec^{-2} within ∼ 200 kpc. Around M31, the detection limit can be slightly improved from 30.0 mag arcsec^{-2} (estimated for the PAndAS survey; Doliva-Dolinsky et al. 2022) to ∼30.5 mag arcsec^{-2}. In a future project, we will use the detection limits determined here to further predict the luminosity function we can hope to measure within the *CSST* volume by modelling observed satellite populations (Koposov et al. 2008; Drlica-Wagner et al. 2020) from cosmological simulations (e.g. NIHAO; Wang et al. 2015).

As we move further away from the Local Group, the *CSST* survey can still reach the detection limits of $M_{V,\rm lim} = -6.0$, $\mu_{250,\rm lim} \sim 29.5$ mag arcsec^{-2} at the distance of 2 Mpc. It will provide us with the opportunity to discover many field dwarf galaxies expected beyond the sphere of influence of the Local Group. The planned survey has a wide coverage of 17 500 deg^2 (42.4 per cent of the whole sky) that

[2]As mentioned above, the detection limits do not correspond to constant surface brightness limits, hence the need to assume the size of a fairly typical Local Group dwarf galaxy.

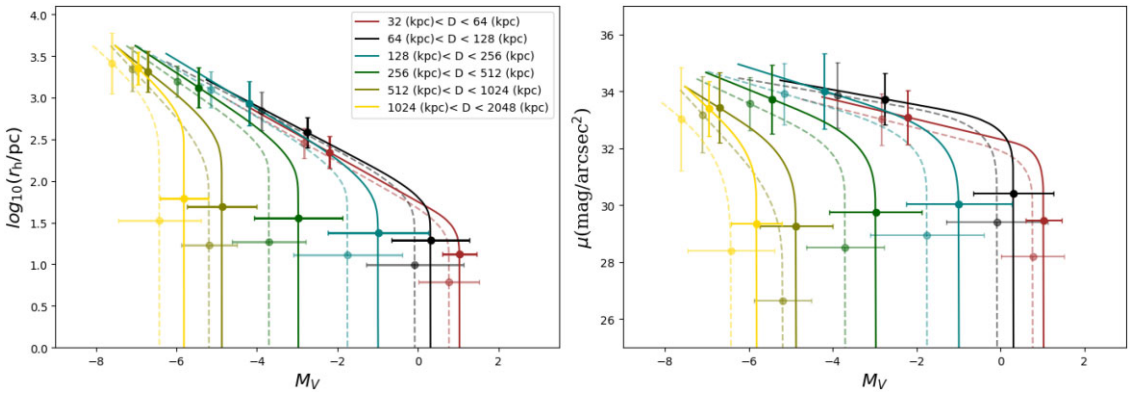

Figure 6. Comparisons of detection limit as a function of M_V and r_h in different distance bins for a M field. Same as Fig. 5, the lines represent the 50 per cent detection fraction, the error bars (σ_M and σ_r) represent difference between 16 per cent and 84 per cent detection fractions. The dashed and solid lines represent the results with single and double exposures, respectively.

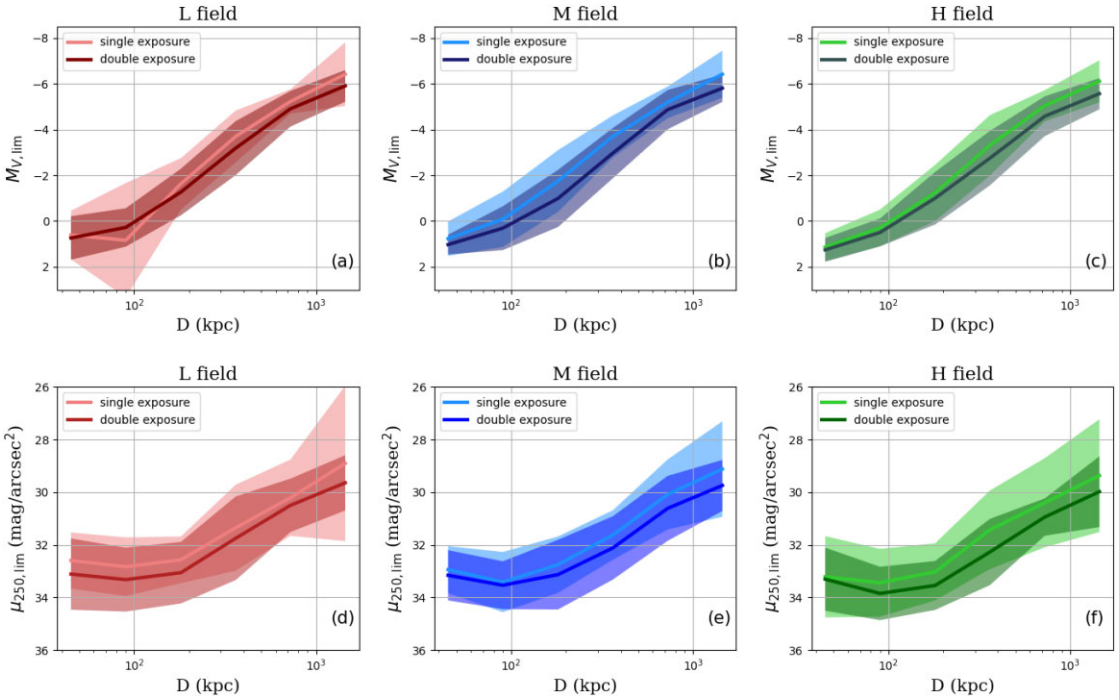

Figure 7. Detection limit of $M_{V,\mathrm{lim}}$ as a function of distance for the two survey modes in the MW three fields. Top panels: results for the single- (light colour) and double-exposure mode (dark colour) in the L (panel a), M (panel b), and H (panel c) fields. The solid curve and the transparent band represent the mean trend and corresponding width (σ_M). Bottom panels: similar to the top panels but for the surface brightness limits of a galaxy with $r_h = 250$, $\mu_{250,\mathrm{lim}}$. The second exposure yields detection limits that can be up to ∼0.5 mag arcsec^{-2} fainter.

covers part of the northern sky, including M31, and overlaps with the LSST in the South. From this joint effort in dwarf galaxy searches, we will, for the first time, have a sample of low-mass dwarf galaxies beyond the MW-M31 pair that can be directly compared to zoom-in dwarf galaxy simulations (e.g. EDGE; Rey et al. 2019).

ACKNOWLEDGEMENTS

We acknowledge the science research grants from the China Manned Space Project with no. CMS-*CSST*-2021-B03, the cosmology simulation database (CSD) in the National Basic Science Data Center (NBSDC) and its funding NBSDC-DB-10 (no. 2020000088).

ZY, NFM, and RAI acknowledge funding from the Agence Nationale de la Recherche (ANR project ANR-18-CE31-0017) and the European Research Council (ERC) under the European Unions Horizon 2020 research and innovation programme (grant agreement no. 834148). XK acknowledge the support from the National Key Research and Development Program of China (no. 2022YFA1602903), the NSFC (no. 11825303), the China Manned Space project with nos. CMS-*CSST*-2021-A03 and CMS-*CSST*-2021-B01.

DATA AVAILABILITY

There are no new data associated with this article.

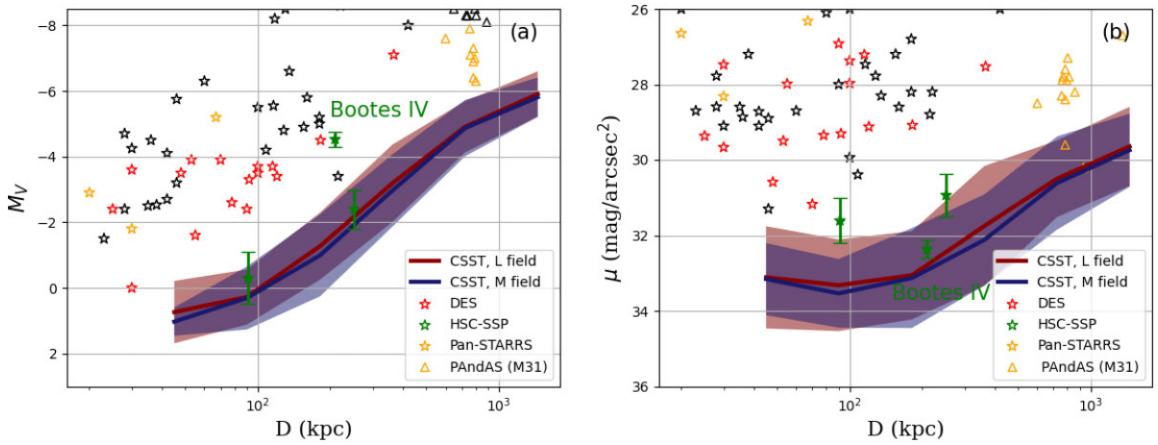

Figure 8. Comparison of the detection limit of *CSST* with known Local Group satellite dwarf galaxies. Panel (a): The solid curves show the detection limits of $M_{V,\rm lim}$ as a function of distance in L (dark red) and M fields (dark blue) and the double-exposure mode, as previous shown in Fig. 6. The star and triangle symbols represent the satellites in the MW and M31, respectively, and are colour-coded according to the survey in which they were discovered. Panel (b): Same as (a) but for the surface brightness limits, $\mu_{250,\rm lim}$ as a function of distance. In both panels, the three newly discovered dwarf galaxies from HSC-SSP are coloured in green with error bars. Boötes IV is located closest to the surface brightness detection limit in (b), but is the most luminous system of these three denoted in (a) as it is also the largest.

Table 3. Detection limits for field M and the double-exposure mode.

D (kpc)	$M_{V,\rm lim}$	$\mu_{250,\rm lim}$ (mag arcsec^{-2})
32–64	1.0	33.2
64–128	0.3	33.5
128–256	− 1.0	33.1
256–512	− 3.0	32.1
512–1024	− 4.9	30.6
1024–2048	− 5.8	29.7

REFERENCES

Abazajian K. et al., 2003, AJ, 126, 2081
Abbott T. M. C. et al., 2018, ApJS, 239, 18
Akeson R. et al., 2019, preprint (arXiv:1902.05569)
Bechtol K. et al., 2015, ApJ, 807, 50
Bertin E., Arnouts S., 1996, A&AS, 117, 393
Bovill M. S., Ricotti M., 2009, ApJ, 693, 1859
Bovill M. S., Ricotti M., 2011, ApJ, 741, 17
Bressan A., Marigo P., Girardi L., Salasnich B., Dal Cero C., Rubele S., Nanni A., 2012, MNRAS, 427, 127
Bullock J. S., Boylan-Kolchin M., 2017, ARA&A, 55, 343
Bullock J. S., Johnston K. V., 2005, ApJ, 635, 931
Cao Y. et al., 2018, MNRAS, 480, 2178
Chambers K. C. et al., 2016, preprint (arXiv:1612.05560)
Doliva-Dolinsky A. et al., 2022, ApJ, 933, 12
Drlica-Wagner A. et al., 2015, ApJ, 813, 109
Drlica-Wagner A. et al., 2020, ApJ, 893, 47
Euclid Collaboration, 2022, A&A, 662, A112
Gong Y. et al., 2019, ApJ, 883, 203
Górski K. M., Hivon E., Banday A. J., Wandelt B. D., Hansen F. K., Reinecke M., Bartelmann M., 2005, ApJ, 622, 759
Homma D. et al., 2016, ApJ, 832, 21
Homma D. et al., 2018, PASJ, 70, S18
Homma D. et al., 2019, PASJ, 71, 94
Ivezić Ž. et al., 2019, ApJ, 873, 111
Kirby E. N., 2009, PhD thesis, Univ. California
Koposov S. et al., 2008, ApJ, 686, 279
Koposov S. E., Belokurov V., Torrealba G., Evans N. W., 2015, ApJ, 805, 130
Lacey C., Cole S., 1993, MNRAS, 262, 627
Laevens B. P. M. et al., 2015a, ApJ, 802, L18
Laevens B. P. M. et al., 2015b, ApJ, 813, 44
Martin N. F. et al., 2013, ApJ, 772, 15
McConnachie A. W. et al., 2018, ApJ, 868, 55
Mau S. et al., 2020, ApJ, 890, 136
Miyazaki S. et al., 2012, in McLean I. S., Ramsay S. K., Takami H., eds, SPIE Conf. Ser. Vol. 8446, Ground-based and Airborne Instrumentation for Astronomy IV. SPIE, Bellingham, p. 9
Pang X.-Y., Olczak C., Guo D.-F., Spurzem R., Kotulla R., 2016, Res. Astron. Astrophys., 16, 37
Phillips J. I., Wheeler C., Cooper M. C., Boylan-Kolchin M., Bullock J. S., Tollerud E., 2015, MNRAS, 447, 698
Rey M. P., Pontzen A., Agertz O., Orkney M. D. A., Read J. I., Saintonge A., Pedersen C., 2019, ApJ, 886, L3
Robin A. C., Reylé C., Derrière S., Picaud S., 2003, A&A, 409, 523
Sharma S., Bland-Hawthorn J., Johnston K. V., Binney J., 2011, ApJ, 730, 3
Sharma S. et al., 2019, MNRAS, 490, 5335
Simon J. D., 2019, ARA&A, 57, 375
Spergel D. et al., 2015, preprint (arXiv:1503.03757)
Vogelsberger M. et al., 2014, MNRAS, 444, 1518
Wallner O., Ergenzinger K., Tuttle S., Vaillon L., Johann U., 2017, in SPIE Conf. Ser. Vol. 10565, EUCLID Mission Design. SPIE, Bellinghaum, p. 122
Walsh S. M., Jerjen H., Willman B., 2007, ApJ, 662, L83
Walsh S. M., Willman B., Jerjen H., 2009, AJ, 137, 450
Wang L., Dutton A. A., Stinson G. S., Macciò A. V., Penzo C., Kang X., Keller B. W., Wadsley J., 2015, MNRAS, 454, 83
Zhan H., 2011, Sci. Sin. Physica, Mechanica and Astronomica, 41, 1441

APPENDIX A: MODEL PARAMETERS

Table A1. Model parameters of detectivity distribution in L field.

D (kpc)	$M_{V,\mathrm{lim}}$	$\log_{10}(r_0)$	β	σ_{M}	σ_{r}
Single exposure					
32–64	0.61	1.45	0.27	1.06	0.21
64–128	0.84	1.42	0.28	2.5	0.22
128–256	− 1.63	2.03	0.28	1.12	0.18
256–512	− 3.7	2.34	0.32	1.13	0.33
512–1024	− 5.23	2.53	0.39	0.53	0.29
1024–2048	− 6.42	2.72	0.46	1.39	0.59
Double exposure					
32–64	0.74	1.58	0.26	0.95	0.27
64–128	0.28	1.70	0.28	0.84	0.24
128–256	− 1.27	2.05	0.29	1.02	0.23
256–512	− 3.19	2.26	0.36	1.18	0.32
512–1024	− 4.91	2.47	0.45	0.78	0.20
1024–2048	− 5.91	2.82	0.41	0.69	0.21

Table A2. Model parameters of detectivity distribution in M field.

D (kpc)	$M_{V,\mathrm{lim}}$	$\log_{10}(r_0)$	β	σ_{M}	σ_{r}
Single exposure					
32–64	0.77	1.47	0.27	0.75	0.18
64–128	− 0.08	1.88	0.25	1.21	0.23
128–256	− 1.75	2.13	0.29	1.35	0.21
256–512	− 3.70	2.43	0.34	0.92	0.19
512–1024	− 5.19	2.35	0.52	0.69	0.27
1024–2048	− 6.42	2.95	0.41	1.03	0.36
Double exposure					
32–64	1.03	1.47	0.27	0.43	0.19
64–128	0.31	1.81	0.25	0.96	0.18
128–256	− 0.99	1.99	0.29	1.25	0.27
256–512	− 2.97	2.33	0.32	1.10	0.24
512–1024	− 4.87	2.61	0.38	0.86	0.25
1024–2048	− 5.81	2.81	0.48	0.60	0.19

Table A3. Model parameters of detectivity distribution in H field.

D (kpc)	$M_{V,\mathrm{lim}}$	$\log_{10}(r_0)$	β	σ_{M}	σ_{r}
Single exposure					
32–64	1.14	1.48	0.26	0.61	0.31
64–128	0.30	1.71	0.28	0.80	0.26
128–256	− 1.23	2.01	0.31	1.23	0.22
256–512	− 3.31	2.15	0.39	1.32	0.30
512–1024	− 5.04	2.59	0.41	0.68	0.34
1024–2048	− 6.11	2.78	0.44	0.92	0.43
Double exposure					
32–64	1.26	1.52	0.25	0.52	0.24
64–128	0.50	1.83	0.26	0.61	0.20
128–256	− 1.00	2.15	0.27	1.15	0.19
256–512	− 2.75	2.30	0.33	1.19	0.25
512–1024	− 4.58	2.57	0.38	0.87	0.14
1024–2048	− 5.57	2.84	0.41	0.68	0.27

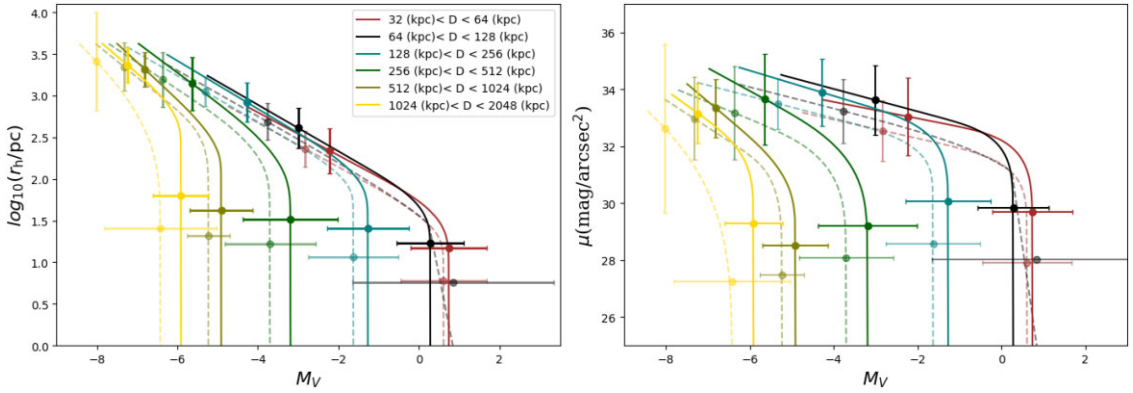

Figure A1. Same as Fig. 6 but for MW field L.

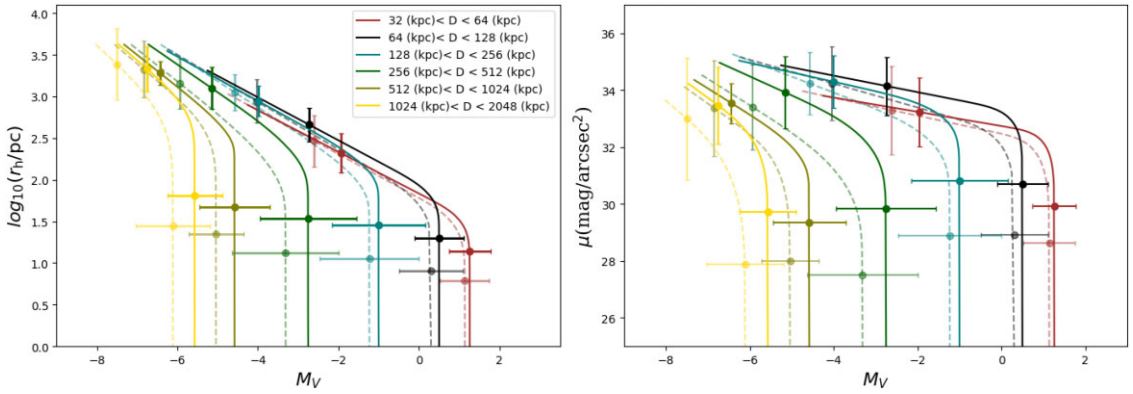

Figure A2. Same as Fig. 6 but for MW field H.

This paper has been typeset from a TEX/LATEX file prepared by the author.